Supplemental Materials

Nonlinear Topological Valley Hall Edge States Arising from Type-II Dirac Cones

Hua Zhong[1,#], Shiqi Xia[2,#], Yiqi Zhang[1,*], Yongdong Li[1], Daohong Song[2,*], Chunliang Liu[1], and Zhigang Chen[2,3,*]

[1]Key Laboratory for Physical Electronics and Devices of the Ministry of Education & Shaanxi Key Lab of Information Photonic Technique, School of Electronic Science and Engineering, Faculty of Electronic and Information Engineering, Xi'an Jiaotong University, Xi'an 710049, China

[2]MOE Key Laboratory of Weak-Light Nonlinear Photonics, TEDA Applied Physics Institute and School of Physics, Nankai University, Tianjin 300457, China

[3]Department of Physics and Astronomy, San Francisco State University, San Francisco, CA 94132, USA

[#]The authors contribute equally to this work

[*]Corresponding authors: zhangyiqi@xjtu.edu.cn, songdaohong@nankai.edu.cn, zhigang@sfsu.edu

1. Design process of type-II Dirac photonic lattices

We summarize the major steps in building up the photonic lattice with type-II Dirac cones as follows:

(1) As shown in Fig. S1, we first obtain a dislocated Lieb lattice by doing a translation operation on the normal uniform Lieb lattice.

(2) We introduce a parametric angle θ in the dislocated Lieb lattice. Clearly, the value of this angle is $\theta = \pi$ in the dislocated Lieb lattice.

(3) We decrease the angle gradually by stretching the lattice along y axis. Examples of such stretched lattices with $\theta = 5\pi/6$, $2\pi/3$, $\pi/2$ and $\pi/3$ are displayed in Fig. S1.

According to our numerical simulations based on both discrete model and continuous model, the lattice with $\theta = \pi/3$ possesses type-II Dirac cones, as shown in Figs. 1(e) and 1(f) in the main text. There are also Dirac cones in lattices with other angles in Fig. S1, but they are all (tilted) type-I Dirac cones.

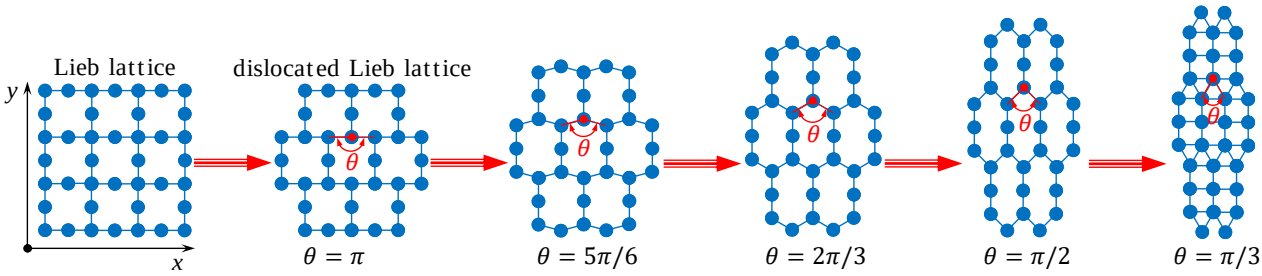

Fig. S1. Construction of the photonic lattice with type-II Dirac cones.

With the decrease of the angle, one finds that the spatial geometry of the lattice changes even though the mirror symmetry along both x and y axes does not change. The appearance of the type-II Dirac cones in the lattice with $\theta = \pi/3$ is mainly due to the anisotropic geometry of the lattice. Under the tight-binding model, the left and right sites aside the red dotted site has no mutual coupling for angles larger than $\pi/3$, but they are coupled when $\theta = \pi/3$. The advantage of the lattice with $\pi/3$ is that the type-II Dirac cone appears naturally without doing extra operations on the lattice or the environment.

2. Other type of domain walls

In the main text, the domain wall is constructed by enhancing the depth of site C of the lattice above the domain wall, while enhancing that of the site A below the domain wall.

Since there are three sites in one unit cell in the lattice with type-II Dirac cones, the domain wall can be also constructed in other way, for example we can decrease the depth of site C above the domain wall, and decrease that the site A below the domain wall. We show the lattices with such a domain wall and corresponding band structure in Fig. S2(a), where a VHE state is found in the second gap. For direct comparison, the lattice with a domain wall used in the main text and its corresponding band structure are shown in Fig. S2(b) – with the VHE state residing in the first band gap. One can find that the VHE state may appear either in the first band gap or in the second band gap, which depends on the way how to break the inversion symmetry of the lattice.

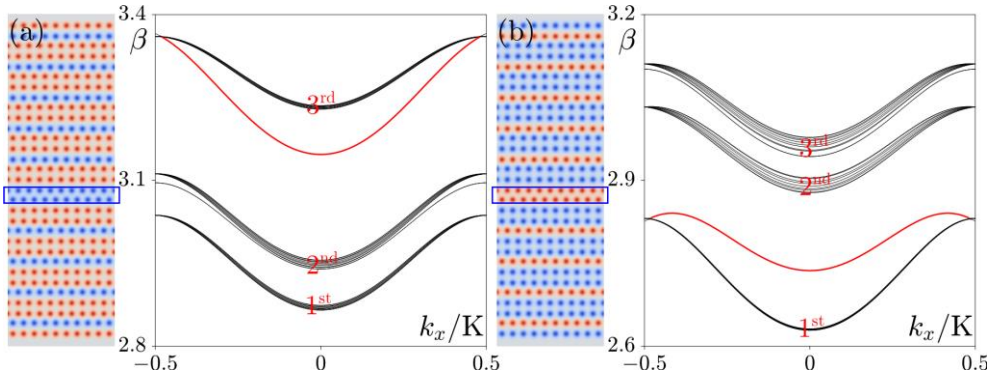

Fig. S2. (a) A domain wall (indicated by a blue rectangle) is built up in the lattice with the index potential of site C decreased above the domain wall and that of site A decreased below the domain wall. The corresponding band structure is shown on its right. (b) Setup is as the same as in (a), but with the corresponding index potential increased instead, as used in the main text.

3. Robustness of the VHE solitons

The topological protection of VHE solitons should be demonstrated by propagating them to circumvent sharp corners. However, it is impossible for us to construct a domain wall with sharp corners without changing the geometry of the lattice, since it is lack of C_{3v} symmetry. A tiny changing of the geometry of the lattice plays a role of defect, which will lead to strong inter-valley scattering of the edge state (as well known, the topological valley protection is fragile, which is a drawback of the valley Hall topological states). As a result, it is very hard for us to check its topological protection directly in the lattice adopted in our manuscript (for the honeycomb lattice, it is not hard to do such checking but we cannot find VHE solitons in honeycomb lattices as of yet). Bearing in mind the formation of the VHE

soliton, we know that it must bifurcate from the linear VHE state and it therefore inherits topological protection from the linear VHE state.

As said, a defect will lead to large inter-valley scattering (reflection) of the VHE solitons, and the reason is that the defect is a small-scale disorder. Therefore, we would like to use a large-scale random disorder to check the robustness of the VHE soliton. The lattice with a large-scale random disorder can be written as $\mathcal{R}(x,y) = \sum_{n,m}\{p_{\text{in}} + \delta_p[1-\cos(\omega x_n)]\}\mathcal{Q}(x-x_n, y-y_m)$ with $\delta_p = 0.01$ and $\omega = 2\pi/100x_m$. Here, the period of the random noise ($100x_m$) is large enough, so that it will not induce inter-valley scattering in a quite long propagate distance which indicates the robustness of such VHE solitons to structure disorder, as shown in Fig. S3 and discussed in the main text.

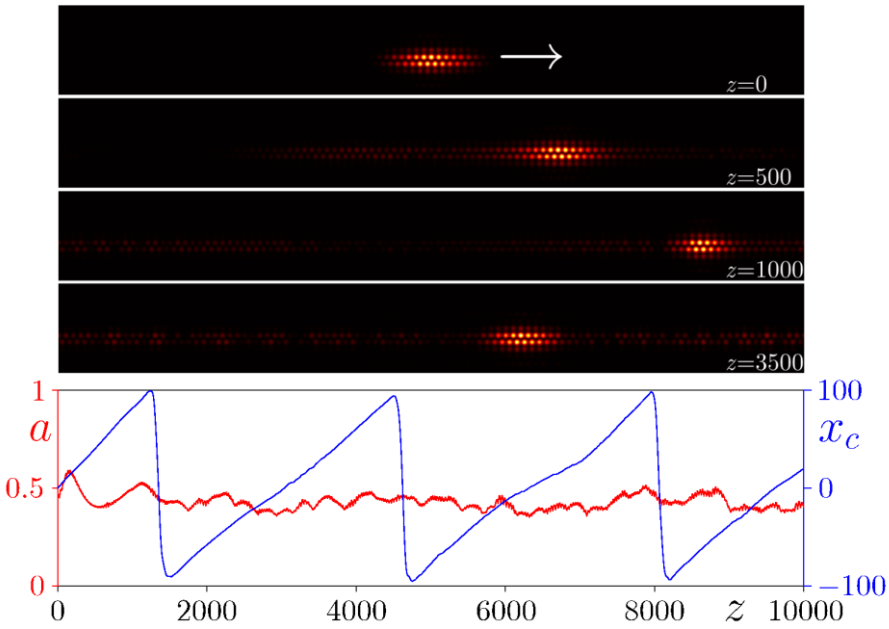

Fig. S3. Propagation of the quasi-soliton in the lattice with a large-scale random disorder. The curves in the bottom panel show the peak amplitude and barycenter of the spot during propagation.

As to the details of the numerical simulation methods adopted in this work including the plane-wave expansion method, the Newton method and the beam propagation method, one can turn to a text book entitled "*Nonlinear Waves in Integrable and Nonintegrable Systems*" written by Jianke Yang.

4. Numerical simulation corresponding to experimental results

We numerically simulated the linear and nonlinear beam dynamics described by Eq. (1) in the main text using the beam propagation method. The parameters are the same as the ones addressed in the main text, i.e. $\Delta n \sim 1.82 \times 10^{-4}$, spacing between nearest neighbor is $d = 30\ \mu$m, etc.. Results shown in Figs. S4(a-c) are corresponding to the experimental results presented in Figs. 4(b-d) of the main text. In agreement with experiment results in Fig. 4, the probe beam at the output is localized in vertical direction and somewhat extended along the domain wall (Fig. S4). Dashed ovals in Fig. S4 indicate the initial

positions of the input beam. Take Fig. S4(a) as an example: the linear output shown in Fig. S4(a1) has a slight shifting to the left denoted by the white arrow, as the experiment results shown in Figs. 4(b1,e1). In the nonlinear condition, the numerical results [Figs. S4(a2,d2)] also agree with experimental observation shown in [Figs. 4(b2,e2)] of the main text, with "diminished" portion in the initial beam due to nonlinearity-induced transport of the nonlinear VHE state. Similar shifting trend happens to the case when the excitation is initially to the right side [Figs. S4(c1,c2,d4)]. Furthermore, the simulated FWHM (see right panels) and the k-space spectra (Figs. S4(a3-c3,a4-c4) all agree well with experiment results shown in Fig. 4 in the main text.

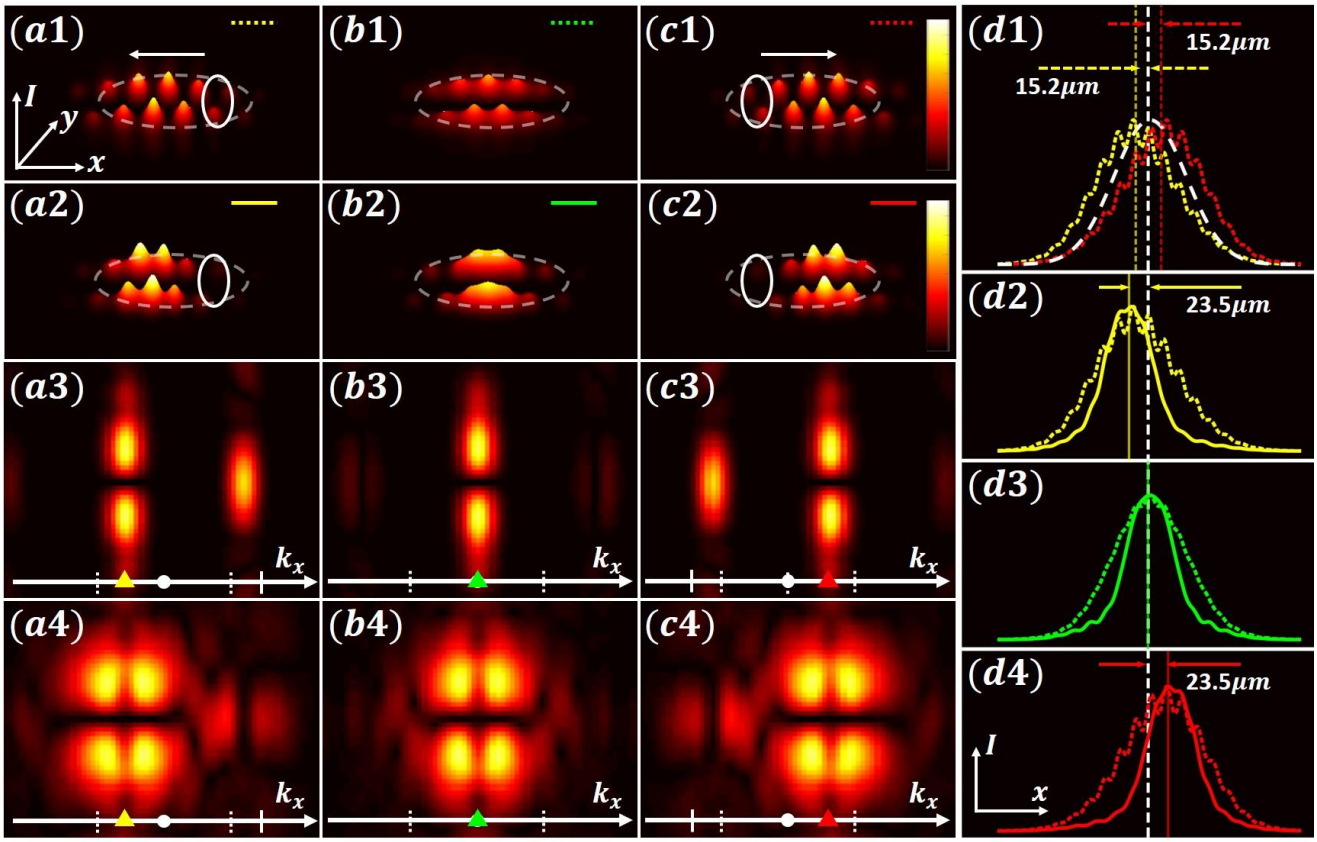

Fig. S4. Numerical simulations of linear (a1-d1, a3-c3) and nonlinear (a2-c2, a4-c4, d2-d4) topological VHE states. The figure layout (a-d) is the same as that for Figs. 4 (b-e) in the main text.

5. Experimental setup and description

In our experiment, a continuous-wave (cw) laser beam (532nm, 50mW) is used to illuminate a programmable phase-only spatial light modulator (SLM). The SLM generates a set of Gaussian beams based on uploaded masks as the writing beams. The waist position of the writing beams is set to the center of crystal along z-direction (Fig. S5). The transverse position and dwelling time of the writing and probe beams are precisely controlled by the SLM. When a bias electric DC field is added along the crystalline c-axis of the nonlinear SBN crystal, due to the self-focusing photorefractive nonlinearity and the memory effect of the crystal, the Gaussian beams induce waveguides one-by-one, and all waveguides

remain intact within the experimental data acquisition period. The strength of the nonlinearity can be well controlled by the dwelling time of probe beams, while the voltage and intensity of the probe beams are fixed. By carefully control the writing time for different sets of the sublattices, we can established the photonic lattices and domain walls with desired index potential as used for our experimental studies.

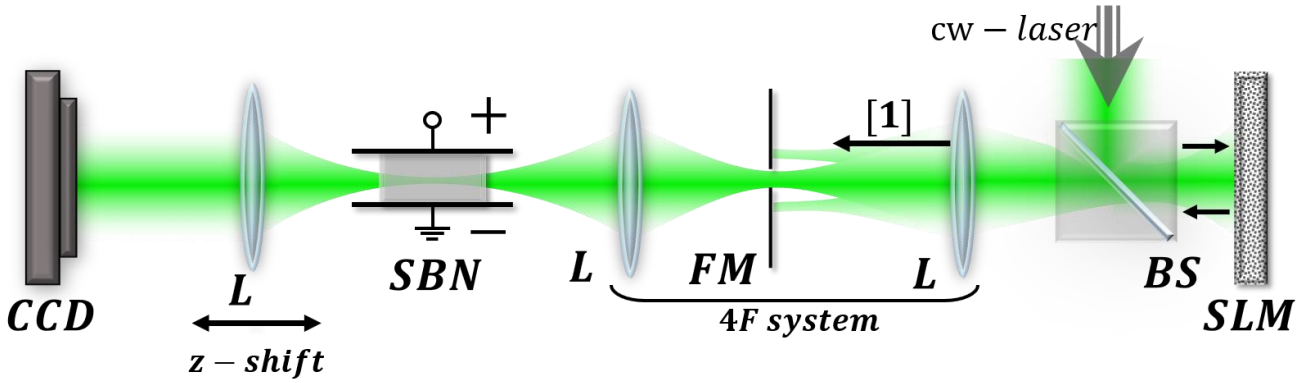

FIG. S5. Experimental setup for point-to-point writing of photonic lattices with a cw-laser (532nm) in a nonlinear photorefractive crystal (SBN: strontium barium niobate crystal). SLM: spatial light modulator; BS: beam splitter; FM: Fourier mask; Path 1 is for both the writing beam and the probe beam, which are launched in sequence.